



## Two-DoF turret mechanism for a rope-driven wheel-legged climbing robot on a 3D façade

Sahoong Ahn <sup>a,1</sup>, DongGuen Hyun <sup>a,1</sup>, Yecheol Moon <sup>a</sup>, Jongmyeong Lee <sup>a</sup>, HwaSoo Kim <sup>b</sup>, TaeWon Seo <sup>a,\*</sup>

<sup>a</sup> Department of Mechanical Convergence Engineering, Hanyang University, Republic of Korea

<sup>b</sup> Department of Mechanical Engineering, Kyunggi University, Republic of Korea

### ARTICLE INFO

**Keywords:**

Climbing robot  
Rope-based robot  
Wheel leg  
Center of gravity control  
Zero-moment point control

### ABSTRACT

Current climbing robots for building cleaning and inspection are typically designed for vertical walls. In this study, a novel robot platform is developed to navigate complex 3D building façades with obstacles and slopes. This platform uses an Ascender, equipped with a winch for climbing, and a wheel-legged mechanism for versatile movement. A linear sliding turret (LST) mechanism is introduced to address challenges encountered with Ascender and wheel-legged mechanisms on three-dimensional façades. By controlling the robot's center of gravity, the LST mechanism distributes ground reaction forces (GRFs) across four legs, minimizing damage to the building. It also controls the zero-moment point (ZMP) and tension to stably overcome obstacles. Experimental validation confirmed the robot's stability on various slopes, obstacle negotiation, and balanced GRF distribution. This rope-driven, wheel-legged climbing robot with an LST mechanism demonstrates strong potential for overcoming challenges in diverse, sloped environments.

### 1. Introduction

Three dimensional (3D) buildings with the purpose of pursuing formative beauty are being built in modern cities [1,2]. Accordingly, the management of the façades of these buildings is attracting increased attention [3,4]. Because of danger to workers, many studies have been conducted on managing façades using robots [5,6]. Among them, the wired and roped methods exhibit high mobility without restrictions on the material or condition of the façade surface [7–9].

Wired and roped methods can be classified into three categories. First, multiple cooperation methods support each other by connecting several robots using ropes and moving façade [10,11]. If a building is extremely large, they are not suitable and require a large number of robots. Second, external winch-type robots [12,13] require winch equipment such as a gantry or gondola on the roof of the building for installation. The installation of the winch equipment is restricted by the weight limit of the roof. Third, built-in winch methods, called ascender types, are very simple to install as they can be operated simply by fixing the rope to a small anchor located on top of the building [14,15]. In addition, using two or more ascenders, a robot can move vertically and horizontally [16] (see Fig. 1).

Ascender-type climbing robots (ATCRs) are difficult to apply to the façades of 3D buildings, such as atypical shapes or domes. ATCRs use

the tension of the rope for movement. In low-slope environments, such as the top of a domed building, the low tension acting on the robot reduces its mobility. They are also limited by their inability to overcome obstacles, such as snow guards and gutters on façades. Relatively low-height obstacles can be overcome using additional mechanisms [17]. As noted in a review paper [7], 96% of obstacles found in buildings are below 500 mm in height; thus overcoming high obstacles remains challenging. Additionally, for stable operation on façades, the base equipped with the working device must be able to maintain an arbitrary target position and orientation; however ATCRs' performance is limited by mechanical constraints. As a result, a mechanism capable of performing movement in low-slope environments, obstacle overcoming and base control is required for use on building façades.

Wheel-legged mechanisms can overcome obstacles with dynamic motion capabilities and excellent mobility in various environments [18, 19]. The wheels of such mechanisms exhibit good mobility, stability, and energy efficiency [20,21] operating based on the frictional force generated by the normal force. In low-slope environments, the normal force exerts a more significant influence than rope tension, thus enabling the wheel mechanism to drive the robot more effectively. Furthermore, soft-tire wheels rarely damage façade surface [22]. A 3-DoF leg mechanism was employed for each of the four legs to (1)

\* Corresponding author.

E-mail address: [taewonseo@hanyang.ac.kr](mailto:taewonseo@hanyang.ac.kr) (T. Seo).

<sup>1</sup> Contributed equally as a first author to this work.

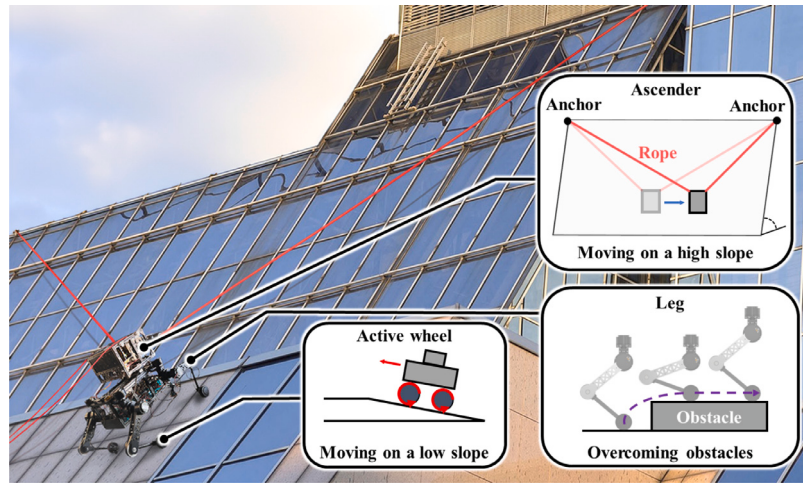


Fig. 1. Rope-driven wheel-legged climbing robot.

overcome obstacles [23,24], (2) control the position and orientation of the robot base, and (3) align the direction of the wheels with the movement direction of the robot. As mentioned earlier, since obstacles in buildings are up to 500 mm in height, the length of the legs needs to be increased to overcome these obstacles, which also results in a higher torque requirement for the motors. Under the condition of constant velocity, insect-type legs consume less energy [25], which implies that they require less torque compared to mammal-type legs. This is because motors with a vertical axis of rotation relative to the ground require lower output torque. Additionally, insect-type legs have a wide workspace, making foot trajectory for obstacle overcoming easier and providing high stability and terrain adaptability [26], which is why they are commonly used in climbing robots [27,28]. Furthermore, it is possible to align the direction of the wheels with the movement direction of the robot by utilizing motors with a vertical axis of rotation relative to the ground. Wheel-legged insect type mechanisms utilize the advantages of both systems to achieve optimal results [22, 29]. Accordingly, in this study, a rope-driven wheel-legged robot with an insect-type mechanism [30] was used as a moving mechanism to overcome the limitations of the ATCR [31] on a 3D building façade.

Since the robot is intended to replace façade workers, the goal is to equip it with the tools used by workers and follow the actual work sequence. As façade work is typically carried out in the vertical direction, the robot's main focus will be on vertical movement and obstacle overcoming, while horizontal movement will be performed primarily for transitioning between multiple vertically extended work areas that are aligned horizontally. When the robot moves or overcomes obstacles, major issues arise in each specific situation.

First, during vertical movement, the wheel-leg mechanism performs the task of fixing the position and orientation of the robot base to the target values for the work, while also aligning the direction of the wheels according to the movement direction. The posture of the wheel-leg can cause the load to concentrate on specific legs due to the tension in the rope and the slope, especially with the forward-tipping moment generated by the tension focusing the load on the front legs. If the load is concentrated, it may cause the robot's feet to lift during movement, leading to instability. This could also result in damage to the building and affect the durability of the robot. The wheel-leg mechanism handles wheel alignment and base stabilization, which limits its movement. Therefore, a separate mechanism is needed to distribute the vertical load.

Secondly, when overcoming obstacles in the vertical direction, the robot uses a method where it lifts one leg at a time. Since the stability of the robot significantly decreases when it is supported by three legs while lifting one, the ZMP must be kept within the support polygon to ensure stability. Factors that affect the ZMP position are the center

of gravity and the rope tension. Although adjusting the posture of the wheel-leg mechanism can shift the ZMP, this can cause interference with the rope, so a mechanism that minimizes posture changes while adjusting the center of gravity and tension to control the ZMP is required.

To address the instability that occurs during vertical movement and obstacle overcoming without using the wheel-leg mechanism, this study utilized a linear sliding turret (LST) mechanism. The LST mechanism creates 2-DoF relative movement between the ascender module and the wheel-leg module. It allows for adjusting the center of gravity through vertical movement and altering the rope tension through rotational movement. The climbing robot system is shown in Fig. 2. The two main contributions of this study can be summarized as follows:

(1) The LST mechanism's vertical translational motion is utilized to shift the center of gravity, enabling vertical load distribution to enhance the robot's stability and protect the durability of both the building and the robot.

(2) The LST mechanism allows for the adjustment of the center of gravity through vertical translational motion and the alteration of rope tension through rotational motion, ultimately enabling the ZMP to be modified. This helps maintain stability in the three-leg support situation that occurs during the obstacle-overcoming process.

The remainder of this paper is organized as follows. In Section 2, the 3D environment in which the robot climbs is defined and the problems that arise in the target environment are analyzed. The LST mechanism is discussed in Section 3. Control strategies in the target environment and the reliability of the robot overcoming obstacles are discussed in Section 4. In Section 5, these aspects are verified through experimental results.

## 2. Target environment analysis

3D building structures have a curvature or various slopes, while obstacles hinder the movement of robots. Before generalization, this study aimed to climb the Gocheok Sky Dome (GSD) [32] in Seoul, Korea (Fig. 3), targeting 3D façade environments with convex surfaces and various high-height obstacles.

The GSD is a semi-elliptical stadium with a height of 67.59 m and a total floor area of 83,623 m<sup>2</sup>, and the minimum curvature of the façade is approximately 4.7 m. On the façade, there are obstacles that robots need to overcome, such as gutters and snow guards, and they are approximately 150–300 mm high. The lower part of the GSD is built with reinforced concrete, and the facade is made of galvanized steel. The surface of the galvanized steel plate is coated with paint and a waterproof coating, and the maximum allowable load is 80 kg. GSD-related information was provided by the Seoul Facilities Corporation [33].

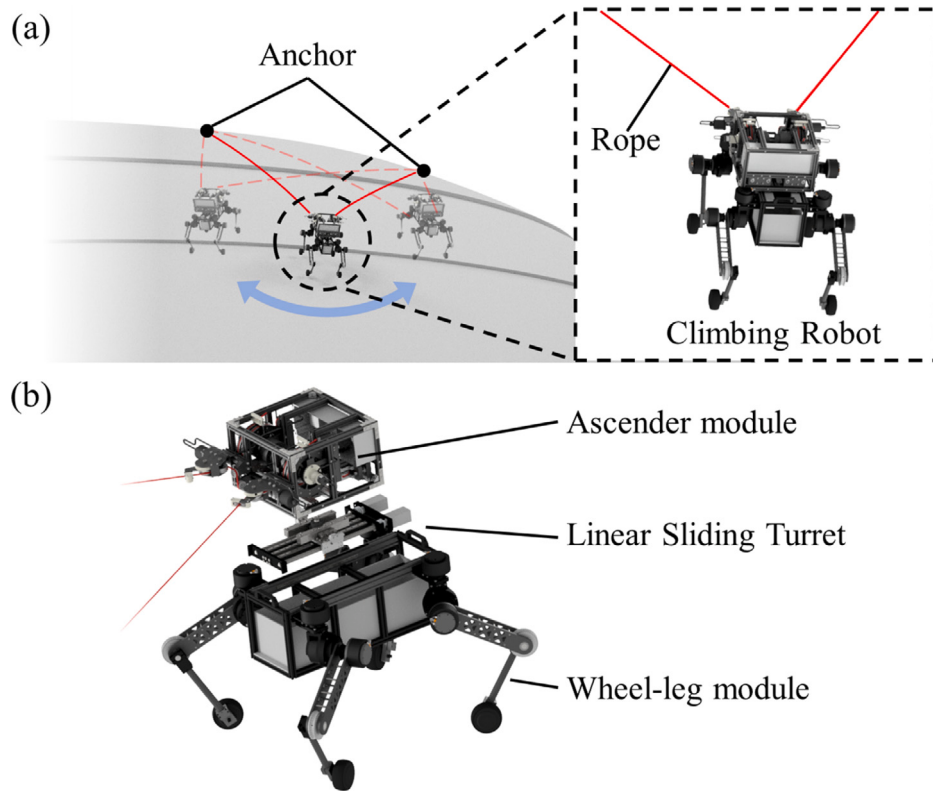


Fig. 2. Climbing robot system configuration.

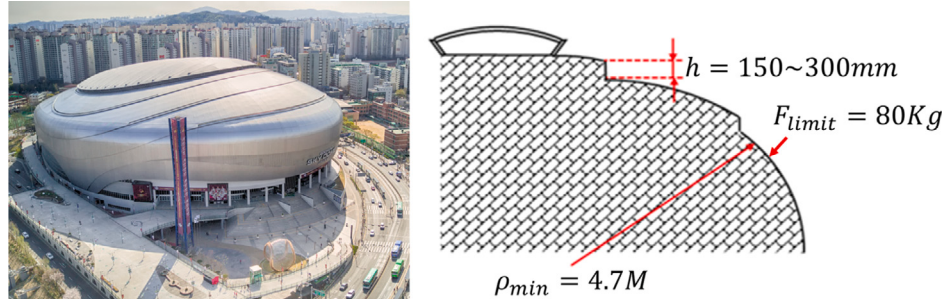


Fig. 3. Targeted 3D façade: Gocheok Sky Dome ©2015. Seoul Facilities Corporation. All rights reserved.

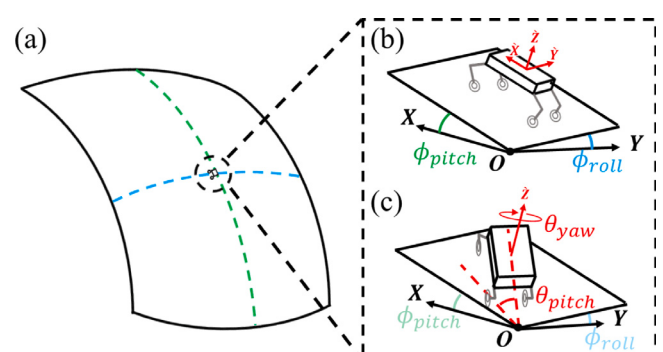
### 2.1. Definition of targeted 3D façade

The GSD has a minimum façade curvature of 4.7 m, which is approximately 7800 times greater than the length or width of the robot (length: 600 mm; width: 550 mm when the robot is in a standard operating position). In this case, the robot can be approximated as a point on a curved surface, and the curved surface at the point where the robot is located can be approximated as a plane [31,34]. The approximated plane is a plane with roll( $\phi_{roll}$ ) and pitch( $\phi_{pitch}$ ) angles, depending on the horizontal and longitudinal curvatures of the curved surface and the position of the robot. In addition, if the robot rotates in the  $\theta_{yaw}$  direction, it is located on a plane in which only the pitch( $\theta_{pitch}$ ) changes. This process is illustrated in Fig. 4.

Fig. 5 shows a schematic of the robot placed on the GSD façade surface. The robot moves along a plane at various angles using two ropes fixed to anchors.

In order to be placed at a certain point, the robot must be able to achieve static equilibrium. The equilibrium equation is as follows:

$$\sum_{i=1}^4 \mathbf{R}_i + \sum_{j=1}^2 \mathbf{T}_j + M\mathbf{g} = \mathbf{0} \quad (1)$$

Fig. 4. Approximation of a curved surface to a plane. (a) Robot on a large-scale curved surface. (b) Plane with a roll( $\phi_{roll}$ ) and pitch( $\phi_{pitch}$ ) angle. These are absolute frame. (c) Plane with a pitch( $\theta_{pitch}$ ) angle. It is relative frame.

where  $\mathbf{R}_i$  is the GRF vector,  $\mathbf{T}_j$  is the tension vector of the rope,  $M$  is the mass of the robot,  $\mathbf{g}$  is the gravitational acceleration,  $\theta_{slope}$  is the

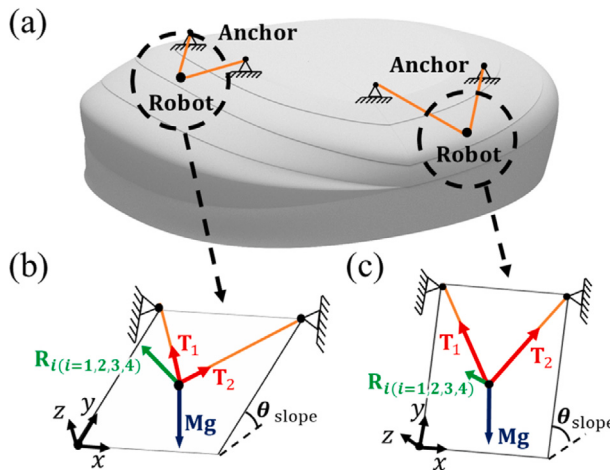


**Fig. 5.** Schematic for the static analysis when the robot moves on a plane at various angles. (a) Robot on the GSD façade surface. (b) Robot on a low-slope plane. (c) Robot on a high-slope plane.

angle of the plane in which the robot is located. The lower  $\theta_{slope}$ , the more dominant the sum of the GRFs acting on the robot is compared to the sum of the tension. This angle is defined as a low slope. A high slope is the angle at which the sum of tension is dominant.

## 2.2. Problem definition of targeted environment

Several problems must be addressed to enable the robot to move reliably in the target environment. The problems are illustrated in Fig. 6.

First, when the robot is on uneven terrain or an external force such as tension is applied, both the robot's load (75 kg) and the dynamic load ( $M_d$ ) may be concentrated at one point on a specific leg owing to the movement of the robot. The result is  $R > F_{limit}$ , which can cause an excessive load on the façade given that the maximum load of the material constituting the façade is 80 kg. This problem not only affects the robot actuator but also causes damage to the façade.

Second, when a strong tension is applied, the moment limits the movement of the front legs of the robot. The moment balance equation for the robot is as follows:

$$\sum_{i=1}^4 (\mathbf{l}_i \times \mathbf{R}_i) + \sum_{j=1}^2 (\mathbf{T}_j \times \mathbf{d}_j) = \mathbf{0} \quad (2)$$

$\mathbf{l}_i$  is the position vector from the CoG to the point where the  $i$ th GRF point and  $\mathbf{d}_j$  is the distance from the CoG to the point where the tension  $\mathbf{T}_j$  acts. Tension  $\mathbf{T}$  is assumed to be equal to the body angle and façade angle. When controlling a robot, the façade angle and the robot angle are controlled to be the same to make it easier to work with the work module that can be attached to the bottom. So the angle of the floor and the body angle are the same. Additionally, the length of the rope is about 5~50 m, which is very long compared to the body size, so the body angle and angles of tension are almost the same. So, we assume that the angles of tension, body angle, and façade angle are the same. To seamlessly integrate the ascender module with the wheel-legged module, it is essential to ensure that the rope of the ascender module and the legs of the wheel do not interfere with each other. To achieve this, the ascender module is connected to the top of the wheel-legged module, and the point of tension is located above the CoG of the robot.

As  $\theta_{slope}$  increases, the tension acting on the robot increases and the moment becomes stronger; thus, the force exerted on the front legs is greater than that on the rear legs. If the force acting on the front legs is too strong, a power greater than the rated torque of the joint motor is required to move the legs. In addition, there is the risk of overturning when the legs move, limiting the movement of the front legs.

## 3. LST mechanism analysis

In this study, an LST mechanism is proposed to solve the defined problems and ensure the robot's stable mobility in the target environment. The LST mechanism improves stability by adding DoF to the ascender module. The rotational DoF enables the robot to rotate in the yaw direction, simplifying the plane on which the robot is located from one with roll and pitch angles to one with only pitch angle. In addition, the LST controls the robot's CoG to properly distribute the GRFs applied to the legs to prevent the load from concentrating on certain parts of the façade on low slopes. Furthermore, it controls the ZMP [35] and rope tension, thereby facilitating overcoming obstacles in various slope environments.

### 3.1. LST mechanism design

The LST consists of transfer and driving units. As shown in Fig. 7(a), the driving unit consists of a motor, a ball screw, and a rack, while the transfer unit consists of the ascender module, a pinion gear, and preload adjuster. The preload adjuster adjusts the clearance such that the power of the driving unit is effectively transmitted to the pinion gear. The LST is firmly fixed to the wheel-leg body frame. The ball screw of the drive unit converts the rotational motion of the motor into the linear motion of the LST block and can withstand high axial loads with a small torque. When the motor is operated, the rack moves linearly and interacts with the pinion. The pinion rotates or moves in a straight line according to the combination of the two motors. The pinion gear is connected to the ascender module; as the pinion moves forward and backward and rotates perpendicular to the ground, the ascender moves or rotates. The linear guide aids in the smooth movement of the pinion. Fig. 7(b) shows the motion of the pinion when the speeds of the two motors are equally controlled. The following is the kinematic equation between the motor input velocity and the output velocity of the LST mechanism.

$$\begin{bmatrix} v_{LST} \\ w_{LST} \end{bmatrix} = \begin{bmatrix} \frac{d_p}{4\pi} & \frac{d_p}{4\pi} \\ -\frac{4\pi}{2\pi r_{gr}} & \frac{4\pi}{2\pi r_{gr}} \end{bmatrix} \begin{bmatrix} q_1 \\ q_2 \end{bmatrix} \quad (3)$$

$v_{LST}$  is linear velocity of LST mechanism and  $w_{LST}$  is angular velocity of LST mechanism.  $d_p$  is the distance the LST motor moves when it rotates one revolution (screw pitch).  $r_{gr}$  is the radius of the central gear of the LST.  $q_1$  and  $q_2$  are the input velocity of the motors in the LST mechanism. The motor's rotational velocity was converted to the guide block velocity of the LST mechanism using the screw pitch  $d_p$  parameter, as shown in Fig. 7. The translational velocity of the LST mechanism was calculated as the average of the velocity of the two guide blocks, while the rotational velocity was determined using the difference between the two block speeds.

### 3.2. Center of gravity control

A leg mechanism robot can move its CoG through a posture change [36,37]. However, the leg mechanism must perform tasks such as aligning the direction of the wheels with the movement direction and fixing the robot's body at the target position and orientation. During obstacle overcoming, it may be limited in movement due to potential interference with the rope. By using the LST mechanism to change the COG (center of gravity) position without relying on the leg mechanism, the aim is to enhance the robot's stability without affecting the performance of the leg mechanism. The translational motion of the LST mechanism creates a relative positional difference between the ascender module and the wheel-leg module, allowing the center of gravity of the ascender module to be shifted, as shown in Fig. 8(a). By changing the center of gravity of the ascender module as shown in the equation below, the overall center of gravity of the robot can be adjusted.

$$y_{CoG,robot} = \frac{m_{ascender}y_{CoG,ascender} + m_{wheelleg}y_{CoG,wheelleg}}{m_{ascender} + m_{wheelleg}} \quad (4)$$

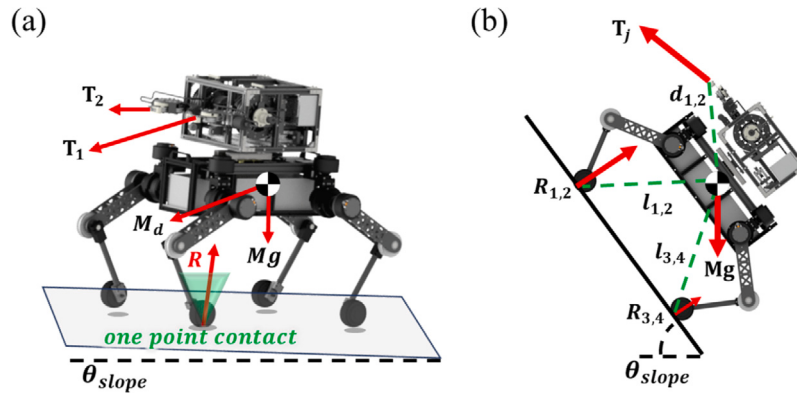


**Fig. 6.** Problems that arise when applying robots to a target environment. (a) One-point contact between the robot and façade in a low-slope environment. (b) Tension-generated moment limits the movement of the front legs.

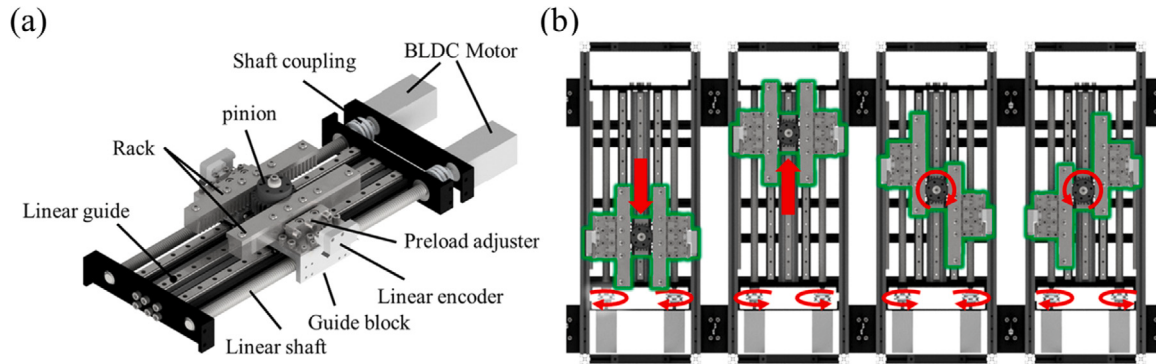


**Fig. 7.** LST mechanism design. (a) LST configuration. (b) Pinion motion according to the motor operating direction.

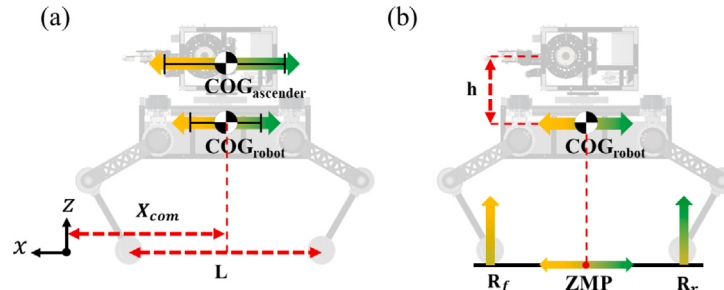


**Fig. 8.** CoG control using the LST. (a) Changes in the CoG due to the ascender module movement. (b) GRF and ZMP control.

This allows control of the GRFs acting on the legs and the ZMP. This process is illustrated in Fig. 8(b).

### 3.3. Tension control

When the leg cannot move due to interference with the rope, the LST mechanism can be used to adjust the tension and modify the ZMP position. The characteristics of the rope affect the robot. Rope characteristics include extension, viscoelasticity, and torsion, and the easiest to model and most influential factor is extension [38]. So, the tension of the rope is modeled and calculated.

The rope can be viewed as a spring in which only tensile force acts upon. The tension can be expressed as follows:

$$T = k\Delta l \quad (5)$$

$k$  is the spring constant of the rope and  $\Delta l$  is the length of the stretched rope. The tension control method is illustrated in Fig. 9, where  $l_1$  and  $l_2$  are the rope lengths between the robot's tension action point and the anchor, respectively. These lengths include the original length of the rope and the extension owing to the load.

However, the rope's characteristics change over time and exhibit nonlinear behavior, making accurate tension control challenging and requiring more in-depth modeling. To address this issue more easily, a module utilizing a load cell is used to measure the rope tension. [31] (see Fig. 10).

The controller receives the target tension value and direction in which to increase the tension. It compares the tension value measured by the load cell installed on the robot with the target tension value and determines the angular velocity of the LST mechanism as a multiple of the difference and constant  $K$ . If the tension to be increased is on

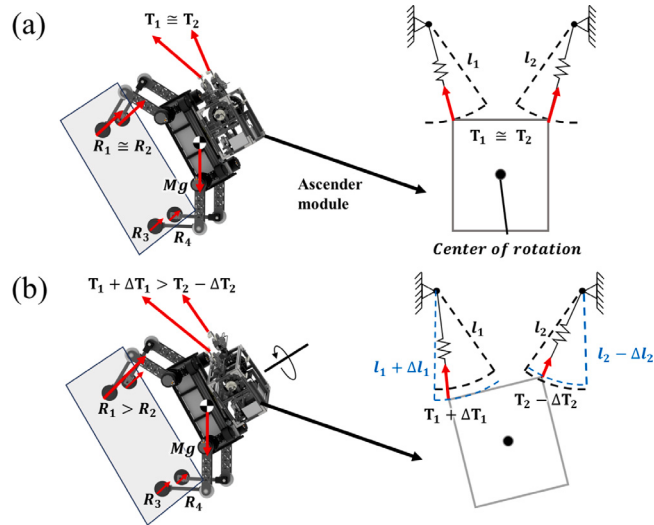


**Fig. 9.** Tension control schematic. (a) Strong force applied to the robot's front legs by the tension in a high-slope environment. (b) LST yaw control for tension control.

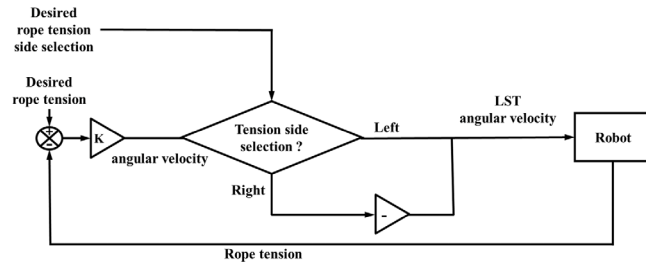


**Fig. 10.** Block diagram for the tension control.

**Table 1**  
Sensor system part list.

Component	Manufacturer	Model
IMU	E2BOX	EBIMU-9DOFv5
BLDC motor	Cubemars	AK80-64
Load cell	CAS	MNT-200 L
Encoder	RLS	AksIM-2

the left rope, it selects forward rotation; if on the right rope, it selects reverse rotation. As a result, the LST mechanism rotates to control the tension until the desired tension is achieved in the specified direction and magnitude.

#### 4. Control strategy for the target environment

##### 4.1. Ground reaction force distribution

When the robot is working on a building, if the load concentrates on a specific leg, the opposing leg is likely to lift due to external forces, leading to system instability. This issue is particularly pronounced when the rope tension generates a forward-tipping moment, frequently causing the load to concentrate on the front legs. To minimize this instability, the ground reaction force on each leg should be distributed with minimal variance. The sum of the reaction forces cannot be reduced because they must be equilibrated with the loads and rope tensions of the robot in arbitrary slope. Therefore, the first goal of the control strategy is to equalize the values of each reaction force using the ground reaction force distribution algorithm (GRFDA). The GRFDA block diagram is shown in Fig. 11.

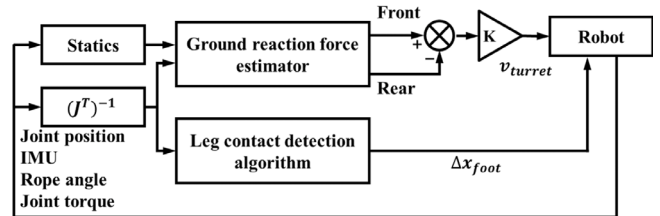


**Fig. 11.** Block diagram for the GRFDA.

The algorithm estimates the ground reaction forces using statics and forward dynamics, then compares the reaction forces between the front and rear legs. Based on the differences, it adjusts the robot's center of gravity through the LST mechanism to redistribute the reaction forces.  $K$  is a control constant that applies output to the LST mechanism in proportion to the difference in the estimated ground reaction forces. Joint positions and joint torques are collected from sensors embedded in the motor drivers, and the rope angle is measured using an encoder-based module, similar to the previous façade cleaning robot [31]. Information related to sensors has been documented in the Table 1. For this method of estimating reaction forces to be conducted accurately, all four feet of the robot must be in contact with the ground. If the estimated GRF value does not exceed a specific threshold, it is determined that the legs are not in contact with the ground. If a leg is determined to not be in contact, the position of the endpoint of the leg is adjusted in a direction perpendicular to the plane in which the robot is located. The plane in which the robot is located is calculated based on an inertial measurement unit (IMU) sensor mounted on the robot's body and kinematic analysis [39]. This process is applied until the estimated ground contact force of the leg exceeds the threshold.

Firstly, it is necessary to estimate the reaction forces at each support point of the robot. Upon conducting a force analysis of the robot, the following expressions can be derived to determine the reaction forces.

$$\sum_{i=1}^4 \mathbf{R}_i = M g \cos \theta_{slope} \quad (6)$$

$$\Sigma \mathbf{R}_{static} = \begin{bmatrix} \Sigma R_f \\ \Sigma R_r \end{bmatrix} = \begin{bmatrix} \frac{Mg}{L} h & \frac{Mg}{L} (x_{CoM}) \\ -\frac{Mg}{L} h & \frac{Mg}{L} (L - x_{CoM}) \end{bmatrix} \begin{bmatrix} \sin \theta_{slope} \\ \cos \theta_{slope} \end{bmatrix} \quad (7)$$

$R_i$  is the each leg's ground reaction force.  $M$  is the total mass (80 kg).  $g$  is the acceleration of gravity.  $\Sigma \mathbf{R}$  is the vector of the reaction force sum,  $\Sigma R_f$ ,  $\Sigma R_r$  are the sum of reaction force front leg, and rear leg respectively.  $h$  is the height difference between the rope exit part and the CoG (0.07 m).  $L$  is the  $x$ -direction distance between wheels (0.4 m).  $x_{CoM}$  is the  $x$ -coordinate of center of mass (CoM).  $\theta$  is the angle of slope.

By adjusting the position of the center of gravity as expressed in Eq. (5), it is possible to vary the reaction forces at the front and rear. If the reaction force at the front is greater, the location of the LST is shifted backward to decrease the center of gravity, thereby reducing the reaction force at the front while increasing the reaction force at the rear. In the force analysis, reaction forces can be determined as in Eq. (5), but dynamic situations are not considered, and uncertainties exist in the force analysis model, leading to draft errors. To address this limitation, estimated reaction forces through motor current measurements are utilized. The characteristics of the motor enable estimation of the torque applied to the motor based on current measurements. Therefore, using the following equation, the torque applied to the motor can be converted into the force acting on the robot's foot.

$$\mathbf{R}_{current} = (\mathbf{J}^T)^{-1} \boldsymbol{\tau}_{joint} \quad (8)$$

$$\mathbf{J} = \begin{bmatrix} l_1 \cos(q_{hr}) + l_2 \cos(q_{hr} - q_k) & -l_2 \cos(q_{hr} - q_k) \\ l_1 \sin(q_{hr}) + l_2 \sin(q_{hr} - q_k) & l_2 \sin(q_{hr} - q_k) \end{bmatrix} \quad (9)$$

$$\mathbf{R}_{estimation} = (1 - \alpha) \mathbf{R}_{static} + \alpha \mathbf{R}_{current} \quad (10)$$

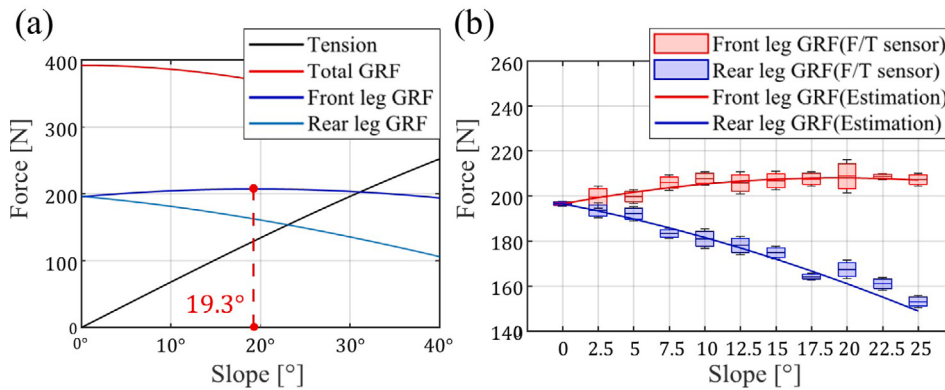


Fig. 12. (a) Analysis of reaction force by slope angle. (b) Experience data of analysis.

$J$  is the Jacobian matrix obtained via kinematic analysis of the leg system.  $q_{hri}$  and  $q_{ki}$  are the joint rotation angles of each motor,  $l_1$  is the distance between the rotation axes of  $q_{hri}$  and  $q_{ki}$ , and  $l_2$  is the distance between  $q_{ki}$  and the end point. As the LST moves rapidly, the dynamic factors become more crucial, thus increasing the weighting factor  $\alpha$  added to the estimated GRF obtained through current measurements.

If all legs are in contact with the ground, the algorithm is executed by comparing the average GRF of the front legs with that of the rear legs. The GRF is properly distributed such that it is not concentrated on one leg by minimizing the difference in the GRF acting on the front and rear legs. This is achieved by moving the CoG in the direction opposite to the side where the GRF is larger. The adjustment process continues until the estimated GRFs for the front and rear legs are equal.

According to Eq. (6), as the slope increases, the total sum of the reaction forces equilibrating the gravitational force in the vertical direction decreases. Additionally, the rope tension equilibrating the gravitational force in the horizontal direction increases. Since the point of application of rope tension is higher than the center of gravity, increasing tension exerts a larger moment on the robot, leading to an increase in the reaction force at the front foot. Ultimately, the reaction force at the front foot is influenced by two factors: the decrease in the total sum of reaction forces due to increasing slope angle, and the increase in tension leading to an increase in the front reaction force. According to the analysis model of the robot, in the range of 19.3 degrees or less, the second factor predominantly affects the increase in reaction force distribution, while beyond this angle, the distribution shows a decrease. In other words, the reaction force at the front foot peaks at 19.3 degrees. On the contrary, the reaction force at the rear foot tends to decrease as the angle increases. This trend is depicted graphically in Fig. 12(a). To verify this trend, the robot in a state where reaction forces are distributed on a plane was subjected to angle changes, and the changes in reaction forces were measured five times each. As shown in Fig. 12(b), the similarity in trends was confirmed. The experimental range for the algorithm was set between 0 degrees, where the total sum of reaction forces is maximum, and 20 degrees, where the reaction force at the front foot reaches its maximum. Experimentation was conducted at angles of 0 degrees, 10 degrees, and 20 degrees. Situations with very high angles were excluded from the experimental range, as illustrated in Fig. 12, where it can be observed that all reaction forces decrease sufficiently. Consequently, the necessity for GRFDA diminishes, hence they were excluded from the experimental range.

#### 4.2. Strategy for overcoming obstacles

To overcome obstacles in a target environment, it is important to ensure stability. We used the ZMP criterion introduced by Vukobratovic [35] to evaluate the robot motion stability. The ZMP criterion states that if the ZMP is within the support polygon made between the

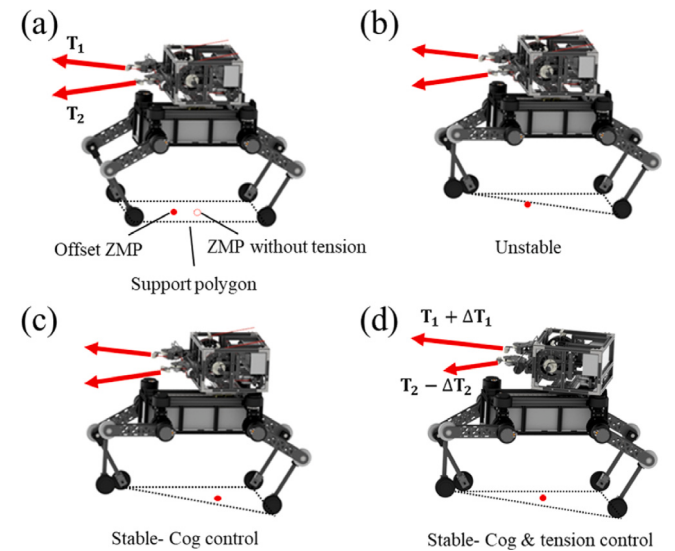


Fig. 13. ZMP control strategy. (a) ZMP when tension is applied. (b) Unstable posture during movement over obstacles. (c) ZMP control using LST on a low slope. (d) ZMP control using LST on a high slope.

robot legs and the ground, then stability is guaranteed [40–43]. For obstacle recognition, a ZED camera is used to measure the distance and height of the obstacle. The appropriate obstacle overcoming algorithm is then selected based on the measured distance and height of the obstacle.

During the process of overcoming obstacles, a critical moment of instability occurs when one of the supporting feet is lifted as shown in Fig. 13(b). To prevent the robot from collapsing, it is essential to position the ZMP within the narrowed support polygon resulting from the reduction in supporting points as shown in Fig. 13(c), (d). Therefore, the second objective of the control strategy focuses on shifting the ZMP into the altered interior of the support polygon during the obstacle overcoming process. The position of the ZMP was calculated separately for the  $x$ -axis and  $y$ -axis, as shown in the Fig. 14. Based on the ZMP location, the position was determined where the sum of the moments caused by tension and gravity becomes zero. The ZMP can be computed as follows:

$$\mathbf{P}_{ZMP} = \begin{bmatrix} x_{ZMP} \\ y_{ZMP} \end{bmatrix} = \begin{bmatrix} \frac{\sum T z_t - M g \sin \theta z_{CoG}}{M g \cos \theta} + x_{CoG} \\ \frac{\sum T z_t}{M g} + y_{CoG} \end{bmatrix} \quad (11)$$

The following equation represents the relationship between the motor input speed and the ZMP movement speed in the LST mechanism,

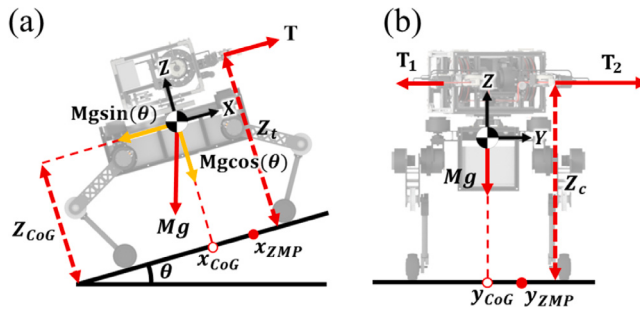


Fig. 14. Schematic for ZMP analysis (a) side view for  $x_{ZMP}$  (b) front view for  $y_{ZMP}$ .

using the screw pitch constant that converts the motor's rotation into the mechanism's translational movement.

$$\begin{bmatrix} \dot{x}_{ZMP} \\ \dot{y}_{ZMP} \end{bmatrix} = \mathbf{AB}\dot{\mathbf{q}}_{LST} = \begin{bmatrix} \frac{m_{asc}}{M} \frac{d_p}{4\pi} & \frac{m_{asc}}{M} \frac{d_p}{4\pi} \\ -\frac{z_k}{Mg} \frac{4\pi}{2\pi r_{gr}} & \frac{z_k}{Mg} \frac{4\pi}{2\pi r_{gr}} \end{bmatrix} \begin{bmatrix} q_1 \\ q_2 \end{bmatrix} \quad (12)$$

Where  $\mathbf{P}_{ZMP} = [x_{ZMP} \ y_{ZMP}]^T$  is ZMP position.  $\mathbf{P}_{CoG} = [x_{CoG} \ y_{CoG} \ z_{CoG}]^T$  is the position of CoG.  $\Sigma T$  and  $\Delta T$  are sum and difference of tensions respectively.  $z_t$  is the distance between the rope exit and the façade.  $m_{asc}$  and  $m_{whl}$  are the mass of ascender and wheel-leg, respectively.  $d_p$  is the distance the LST motor moves when it rotates one revolution (screw pitch).  $r_{gr}$  is the radius of the central gear of the LST.  $\mathbf{A}$ ,  $\mathbf{B}$  are transformation matrix respectively LST velocity to ZMP velocity vector and  $\dot{\mathbf{q}}_{LST}$  to ZMP velocity vector.  $\dot{\mathbf{q}}_{LST} = [q_1 \ q_2]^T$  are the rotational speeds of the LST motor. The maximum speed of ZMP is 498 mm/min, and maximum rotational speed of ZMP is 19 RPM. The workspace of this mechanism is 295 mm and rotation range is 360 degrees.

According to Eq. (11), the x-coordinate of the ZMP is correlated with the x-coordinate of the center of gravity. Utilizing the LST mechanism, as shown in Fig. 13. (c), to manipulate the x-coordinate of the center of gravity, the x-coordinate of the ZMP can be adjusted to enter the support polygon. Similarly, the y-coordinate of the ZMP correlates with the discrepancy in lateral tension affecting the robot. As discussed in Chapter 3's Tension control, employing the rotational shift translation of the LST mechanism can induce tension discrepancies, thereby altering the y-coordinate of the ZMP as shown in Fig. 13. (d). Eq. (10) represents the relationship between the motor input of the LST mechanism and the velocity of ZMP movement. By utilizing this equation, the position of the ZMP can be adjusted to move it within the support polygon.

## 5. Experiment and result

### 5.1. Ground reaction force distribution experiment

In this experiment, the GRFDA was used to ensure that the forces acting on the front and rear legs were properly distributed in a slope environment. The robot is located on various slopes and GRFDA controls the LST transfer unit from the center of the robot body to a position where the GRF error acting on the front and rear legs is zero.

The test bench used in the experiment held the rope at its designated position and changed the pitch angle of the plane in which the robot was located, as shown in Fig. 15. We used specially built legs to evaluate the performance of the robot system and algorithm. The leg was fitted with a 6-axis force torque sensor (BOTA Rokubi 1.3) [44]. The algorithm was executed for slope (0°), (10°), and (20°) where the tension acted.

The experiment was performed five times at each slope. Fig. 16 shows the GRF error acting on the front and rear legs estimated using the GRFDA on each slope and the GRF error acting on the front and

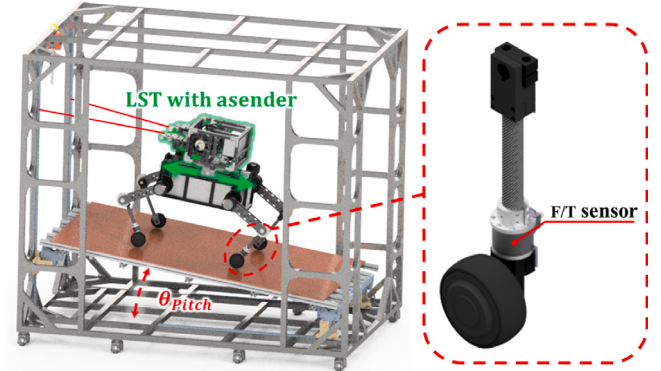


Fig. 15. Configuration of the GRF distribution experiment.

rear legs measured using the sensor. The graph shows the  $\pm 2s$  range of the mean value, where  $s$  is the sample standard deviation. The GRFDA successfully controlled the robot such that the GRF error acting on the front and rear legs at all slopes (i.e., 0°, 10°, and 20°). Although the accuracy of the estimated GRFs was not high, they exhibited the same trend as the GRF measured by the sensor. This prevents the robot's load from being concentrated on a particular leg on slopes where the façade is fully loaded with the robot. As a result, stability on the building façade is ensured.

### 5.2. Obstacle overcoming on various slope

Fig. 17 shows the robot overcoming some obstacles. In the target environment, the slope angle at which the obstacle for the robot to overcome was located was within 10° and 35°. However, to overcome obstacles in more diverse environments, the experiment was conducted on flat (0°), mid-slope (45°), and high-slope (90°) environments. The plane size of test-bench is width 1135 mm, depth 3800 mm. The height is 2805 mm when angle is 45°. The height of the obstacle was 250 mm.

At 0°, no tension is applied. In such an environment, obstacles can be stably overcome by moving the CoG back and forth, as shown in Fig. 13(c). In addition, the legs of the robot can be freely controlled so that a support polygon can be freely formed.

At the 45° slope, the tension acts significantly and a large force is applied to the front legs. When raising the front legs over the obstacle, ZMP is controlled using the CoG and tension control, as shown in Fig. 13(d), and one leg is allowed to move freely. The rear legs do not exert much load; therefore, they only overcome obstacles by moving their CoG.

When the slope angle is extremely high and a very strong tension is applied, the rear legs detach from the plane and the support polygon becomes meaningless. The robot becomes suspended on the rope. When a robot hangs from a rope, it can maintain its overturning stability with only one-point support using its front legs; therefore, when placing the front legs on an obstacle at a 90° slope, a method similar to the 45°-slope case is used. After raising the front legs over the obstacle, the robot moves to a two-point support state to reduce vibration. The GRF does not act on the rear legs; therefore, the robot can freely place the rear legs on the obstacle.

## 6. Conclusion

In this study, we introduced LST, which can improve the limitations of ascender and wheel-leg robot system. We applied an LST mechanism, a 2-DOF turret that introduces linear and rotational DoF to the ascender module. The LST allows control over the robot's center of gravity and, through the GRFDA, effectively prevents the robot from exerting an excessive force on the exterior wall of the building. Moreover,

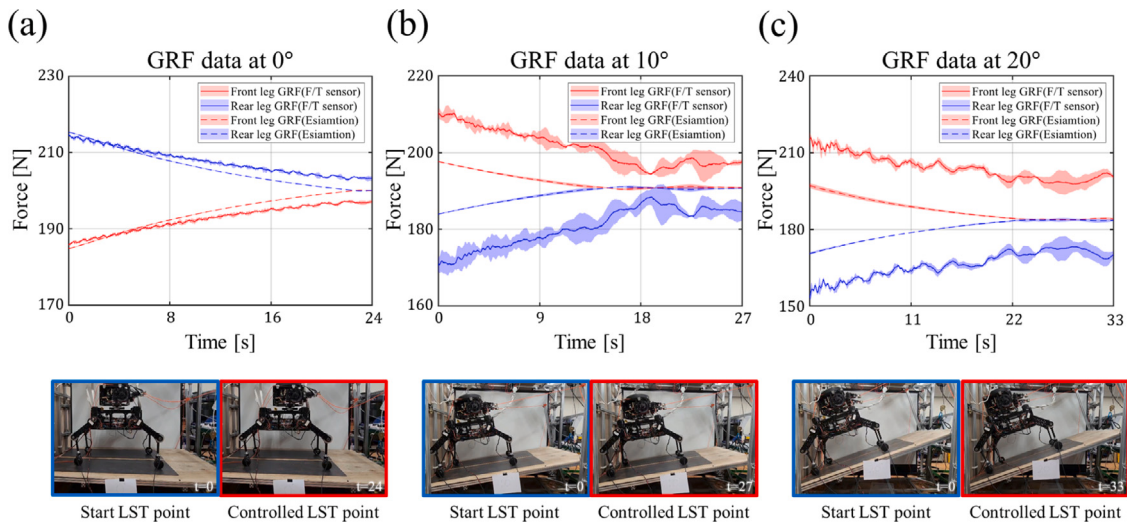


**Fig. 16.** Ground reaction force distribution experimental results. Experimental results at (a) 0°, (b) 10°, and (c) 20°.

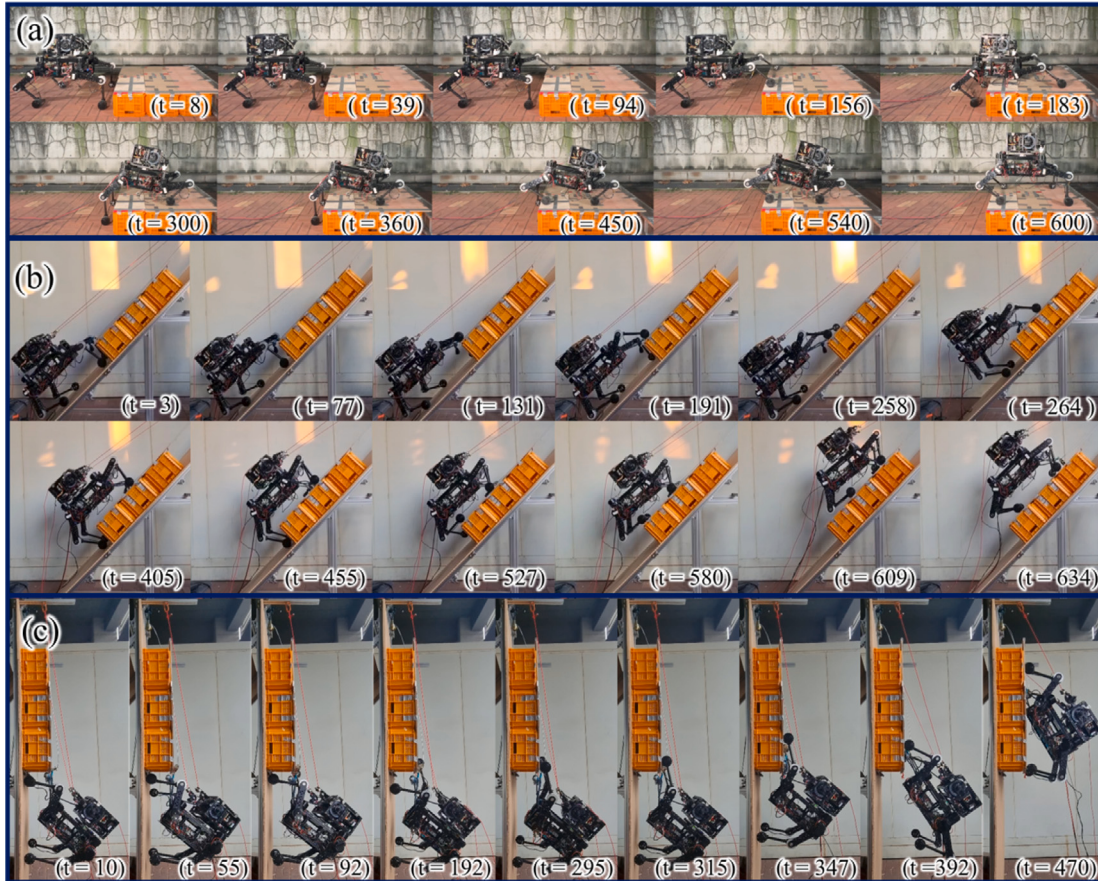


**Fig. 17.** Obstacle overcoming on various slopes. (a) 0°; (b) 45°; and (c) 90°.

by controlling the tension and ZMP, the robot demonstrated stable obstacle overcoming at angles of 0°, 45°, and 90°, indicating that it has the potential to reliably overcome obstacles in various inclined environments between 0° and 90°.

The ultimate goal is to get the robot to perform tasks such as cleaning and inspection in real time in various environments. To this end, future studies will increase the reliability of the robot by estimating the GRF of the proposed system more precisely. We will also study

trajectory planning optimization strategies to improve the ability to overcome high obstacles.

Due to the current limitations of the robot's computational performance, real-time parameter updates using the Kalman filter are not feasible, resulting in lower ground reaction force estimation accuracy. Future research will focus on enhancing the robot's computational capabilities and improving the ground reaction force estimation algorithm using the Kalman filter.

In the current study, vertical movement and obstacle overcoming were prioritized to mimic the working process of human operators. However, to fully leverage the advantages of a robot capable of 2-DoF movement, it must navigate optimally across various directions. Future research will focus on enabling movement and obstacle overcoming in all directions, aiming to propose the optimal path suited for building environments.

This study focuses on the LST mechanism; however, future research will aim to integrate it into the work process of actual robots, implementing it in façade work robot systems. Additionally, the goal is to develop a system where the LST mechanism autonomously operates by recognizing the robot's surrounding environment during tasks.

### CRediT authorship contribution statement

**Sahoон Ahn:** Writing – original draft, Visualization, Validation, Methodology, Investigation, Data curation, Conceptualization. **DongGuen Hyun:** Writing – original draft, Visualization, Validation, Methodology, Investigation, Formal analysis, Data curation, Conceptualization. **Yecheol Moon:** Visualization, Validation, Methodology, Investigation. **Jongmyeong Lee:** Validation, Methodology, Investigation. **HwaSoo Kim:** Funding acquisition, Project administration. **TaeWon Seo:** Writing – review & editing, Project administration, Funding acquisition, Conceptualization.

### Declaration of competing interest

The authors declare that they have no known competing financial interests or personal relationships that could have appeared to influence the work reported in this paper.

### Acknowledgments

This research was supported by the National Research Foundation of Korea (NRF) Grant funded by the Ministry of Science and Bridge Convergence R & D Program (NRF-2021M3C1C3096807, NRF-2021M3C1C3096808). Appreciation for the space rental of Seoul Facilities Corporation. We thank Seoul Facilities Corporation for lending us the space for research.

### Appendix A. Supplementary data

Supplementary material related to this article can be found online at <https://doi.org/10.1016/j.measurement.2024.116073>.

### Data availability

No data was used for the research described in the article.

### References

- [1] K. Volders, Morphological scheme of second-generation non-orthogonal high-rises, in: CTBUH 8th World Congress, 2008.
- [2] T. Al-Azzawi, Z. Al-Majidi, Parametric architecture: the second international style, in: IOP Conference Series: Materials Science and Engineering, vol. 1067, (1) IOP Publishing, 2021, 012019.
- [3] S.-M. Moon, J. Huh, S. Lee, S. Kang, C.-S. Han, D. Hong, A survey on robot systems for high-rise building wall maintenance, *J. Korean Soc. Precis. Eng.* 30 (4) (2013) 359–367.
- [4] Y. Liu, Y. Lin, J.K. Yeoh, D.K. Chua, L.W. Wong, M.H. Ang, W. Lee, M.Y. Chew, Framework for automated UAV-based inspection of external building façades, *Autom. Cities Des. Constr. Oper. Future Impact* (2021) 173–194.
- [5] D. Lattanzi, G. Miller, Review of robotic infrastructure inspection systems, *J. Infrastructure Syst.* 23 (3) (2017) 04017004.
- [6] M.F. Silva, J.T. Machado, J.K. Tar, A survey of technologies for climbing robots adhesion to surfaces, in: 2008 IEEE International Conference on Computational Cybernetics, IEEE, 2008, pp. 127–132.
- [7] T. Seo, Y. Jeon, C. Park, J. Kim, Survey on glass and façade-cleaning robots: Climbing mechanisms, cleaning methods, and applications, *Int. J. Precis. Eng. Manuf.-Green Technol.* 6 (2019) 367–376.
- [8] N. Imaoka, S.-g. Roh, N. Yusuke, S. Hirose, SkyScraper-I: Tethered whole windows cleaning robot, in: 2010 IEEE/RSJ International Conference on Intelligent Robots and Systems, IEEE, 2010, pp. 5460–5465.
- [9] M. Seo, S. Yoo, J. Kim, H.S. Kim, T. Seo, Dual ascender robot with position estimation using angle and length sensors, *IEEE Sens. J.* 20 (13) (2020) 7422–7432.
- [10] A. Nejadfarid, H. Moradi, M.N. Ahmadabadi, A multi-robot system for dome inspection and maintenance: Concept and stability analysis, in: 2011 IEEE International Conference on Robotics and Biomimetics, IEEE, 2011, pp. 853–858.
- [11] K. Naderi, K. Taheri, H. Moradi, M.N. Ahmadabadi, An evolutionary artificial potential field algorithm for stable operation of a multi-robot system on domes, in: 2014 IEEE International Conference on Autonomous Robot Systems and Competitions, ICARSC, IEEE, 2014, pp. 92–97.
- [12] M.A. Armada, P. de González Santos, N. Elkemann, D. Kunst, T. Krueger, M. Lucke, T. Böhme, T. Felsch, T. Stürze, SIRIUSc—Façade cleaning robot for a high-rise building in Munich, Germany, in: Climbing and Walking Robots: Proceedings of the 7th International Conference CLAWAR 2004, Springer, 2005, pp. 1033–1040.
- [13] H. Chae, G. Park, J. Lee, K. Kim, T. Kim, H.S. Kim, T. Seo, Façade cleaning robot with manipulating and sensing devices equipped on a gondola, *IEEE/ASME Trans. Mechatronics* 26 (4) (2021) 1719–1727.
- [14] K. Seo, S. Cho, T. Kim, H.S. Kim, J. Kim, Design and stability analysis of a novel wall-climbing robotic platform (ROPE RIDE), *Mech. Mach. Theory* 70 (2013) 189–208.
- [15] H. Chae, Y. Moon, K. Lee, S. Park, H.S. Kim, T. Seo, A tethered façade cleaning robot based on a dual rope windlass climbing mechanism: Design and experiments, *IEEE/ASME Trans. Mechatronics* 27 (4) (2022) 1982–1989.
- [16] M. Choi, M. Seo, H.S. Kim, T. Seo, Ukf-based sensor fusion method for position estimation of a 2-dof rope driven robot, *IEEE Access* 9 (2021) 12301–12308.
- [17] Y. Lee, M. Seo, S. Ryu, H.S. Kim, T. Seo, Novel mobile mechanism design for an obstacle-overcoming robot using rotating spokes, *IEEE Access* 9 (2021) 122766–122773.
- [18] C. Grand, F. Benamar, F. Plumet, P. Bidaud, Stability and traction optimization of a reconfigurable wheel-legged robot, *Int. J. Robot. Res.* 23 (10–11) (2004) 1041–1058.
- [19] X. Li, H. Zhou, H. Feng, S. Zhang, Y. Fu, Design and experiments of a novel hydraulic wheel-legged robot (WLR), in: 2018 IEEE/RSJ International Conference on Intelligent Robots and Systems, IROS, IEEE, 2018, pp. 3292–3297.
- [20] L. Bai, J. Guan, X. Chen, J. Hou, W. Duan, An optional passive/active transformable wheel-legged mobility concept for search and rescue robots, *Robot. Auton. Syst.* 107 (2018) 145–155.
- [21] L. Bruzzone, P. Fanghella, Mantis: hybrid leg-wheel ground mobile robot, *Ind. Robot. An Int. J.* 41 (1) (2014) 26–36.
- [22] M.H. Salehpour, B. Zamanian, H. Moradi, The design, implementation, and stability analysis of a human-inspired dome-tethered robot, in: 2014 Second RSI/ISM International Conference on Robotics and Mechatronics, ICRoM, IEEE, 2014, pp. 648–653.
- [23] V.G. Loc, T.H. Kang, H.S. Song, H.R. Choi, Gait planning of quadruped walking and climbing robot in convex corner environment, *Inst. Control Robotics Syst.* (2005) 314–319.
- [24] S. Hirose, K. Yoneda, H. Tsukagoshi, TITAN VII: Quadruped walking and manipulating robot on a steep slope, in: Proceedings of International Conference on Robotics and Automation, vol. 1, IEEE, 1997, pp. 494–500.
- [25] S. Hirose, A study of design and control of a quadruped walking vehicle, *Int. J. Robot. Res.* 3 (2) (1984) 113–133, <http://dx.doi.org/10.1177/027836498400300210>.
- [26] S. Kitano, S. Hirose, A. Horigome, G. Endo, TITAN-XIII: sprawling-type quadruped robot with ability of fast and energy-efficient walking, *Robomech. J.* 3 (8) (2016) <http://dx.doi.org/10.1186/s40648-016-0047-1>.
- [27] T. Doi, R. Hodoshima, S. Hirose, Y. Fukuda, T. Okamoto, J. Mori, Development of a quadruped walking robot to work on steep slopes, TITAN XI (walking motion with compensation for compliance), in: 2005 IEEE/RSJ International Conference on Intelligent Robots and Systems, 2005, pp. 2067–2072, <http://dx.doi.org/10.1109/IROS.2005.1545498>.
- [28] Y. Tanaka, Y. Shirai, X. Lin, A. Schperberg, H. Kato, A. Swerdlow, N. Kumagai, D. Hong, SCALER: A tough versatile quadruped free-climber robot, in: 2022 IEEE/RSJ International Conference on Intelligent Robots and Systems, IROS, 2022, pp. 5632–5639, <http://dx.doi.org/10.1109/IROS47612.2022.9981555>.
- [29] M. Kameda, N. Kashiri, N.G. Tsagarakis, On the kinematics of wheeled motion control of a hybrid wheeled-legged centaur robot, in: 2018 IEEE/RSJ International Conference on Intelligent Robots and Systems, IROS, IEEE, 2018, pp. 2426–2433.
- [30] B. Huang, L. Sun, Y. Luo, Statically balanced stair climbing gait research for a hybrid quadruped robot, in: IEEE International Conference Mechatronics and Automation, 2005, vol. 4, IEEE, 2005, pp. 2067–2071.
- [31] K. Lee, S. Ahn, J. Kwon, H.S. Kim, T. Seo, Façade operation robot on convex surface using an embedded rope ascender, *Autom. Constr.* 159 (2024) 105250.

- [32] Introduction to Gocheok Sky Dome. URL [https://www.sisul.or.kr/open\\_content/skydome/introduce/intro.jsp](https://www.sisul.or.kr/open_content/skydome/introduce/intro.jsp).
- [33] Seoul Facilities Corporation. URL [https://www.sisul.or.kr/open\\_content/main/](https://www.sisul.or.kr/open_content/main/).
- [34] D. Son, Mobile robot platform on 3D shape façade using wheel-leg mechanism for rope-based façade robot (Ph.D. thesis), Hanyang University, 2023.
- [35] M. Vukobratović, B. Borovac, Zero-moment point—Thirty five years of its life, *Int. J. Hum. Robotics* 1 (01) (2004) 157–173.
- [36] T. Horvat, K. Melo, A.J. Ijspeert, Model predictive control based framework for com control of a quadruped robot, in: 2017 IEEE/RSJ International Conference on Intelligent Robots and Systems, IROS, IEEE, 2017, pp. 3372–3378.
- [37] L. Sentis, J. Park, O. Khatib, Compliant control of multicontact and center-of-mass behaviors in humanoid robots, *IEEE Trans. Robot.* 26 (3) (2010) 483–501.
- [38] C. Leech, *The Modelling and Analysis of the Mechanics of Ropes*, vol. 209, Springer, 2014.
- [39] C. Gehring, C.D. Bellicoso, S. Coros, M. Bloesch, P. Fankhauser, M. Hutter, R. Siegwart, Dynamic trotting on slopes for quadrupedal robots, in: 2015 IEEE/RSJ International Conference on Intelligent Robots and Systems, IROS, IEEE, 2015, pp. 5129–5135.
- [40] Q. Huang, K. Yokoi, S. Kajita, K. Kaneko, H. Arai, N. Koyachi, K. Tanie, Planning walking patterns for a biped robot, *IEEE Trans. Robot. Autom.* 17 (3) (2001) 280–289.
- [41] R. Mandava, P. Vundavilli, An adaptive PID control algorithm for the two-legged robot walking on a slope, *Neural Comput. Appl.* 32 (2020) 3407–3421, <http://dx.doi.org/10.1007/s00521-019-04326-2>.
- [42] M.S. Khan, R.K. Mandava, Design of dynamically balanced gait for the biped robot while crossing the obstacle, *Proc. Inst. Mech. Eng. C* 238 (18) (2024) 9125–9140, <http://dx.doi.org/10.1177/09544062241246878>.
- [43] R. Mandava, S. Bondada, P. Vundavilli, An optimized path planning for the mobile robot using potential field method and PSO algorithm, *Soft Comput. Probl. Solving Adv. in Intell. Syst. Comput.* 817 (2019) 139–150, [http://dx.doi.org/10.1007/978-981-13-1595-4\\_112](http://dx.doi.org/10.1007/978-981-13-1595-4_112).
- [44] Bota systems 6 Axis Force Torque Sensor. URL <https://www.botasy.com/force-torque-sensors/rokubi>.